Design of Novel High-Efficiency Inverse Class-E Power Amplifier

Akram Sheikhi, *Senior Member, IEEE*, Jiteng Ma, *Member, IEEE*, Andrei Grebennikov, *Senior Member, IEEE*, and Mark Beach, *Senior Member, IEEE*

***Abstract*—In this study, we provide a theoretical examination of an innovative inverse Class-E power amplifier (PA) incorporating a shunt filter to achieve optimal performance. We derive idealized waveforms and load parameters, verifying these through frequency domain simulations. The findings indicate that the performance of inverse Class-E PA does not consistently increase with higher parasitic output capacitance. The ideal switch voltage and current waveforms suggest the potential for reaching 100% efficiency. We offer design examples using both lumped elements and transmission lines. To validate our theoretical predictions, we conducted measurements on the transmission line inverse Class-E. The simulation and measurement results closely align, showing a maximum drain efficiency of 82%/81% and a power-added efficiency of 75%/74.8%. Furthermore, an output power of 40.5/40.3 dBm and a power gain of 11.0/10.3 dB were achieved in the saturation region.**

***Index Terms*—Inverse class-E, shunt filter, zero-current switching (ZCS), zero-derivative current switching (ZDCS).**

I. Introduction

THE power amplifier (PA) plays a crucial role in communication systems by amplifying the signal to a level suitable for transmission or further processing. It is essential in various communication applications, including wireless communication systems, broadcasting, satellite communication, etc. Efficient PAs minimize power losses in the amplification process, resulting in improved energy efficiency and longer battery life in portable communication devices. It has been investigated that the energy consumption of PAs takes around 17% of the total operation energy for communication service providers [1]. Over the past decades, both academic research and industrial developments have focused on improving PA efficiency [2] and designing innovative PA architectures [3], [4] to minimize power consumption and reduce heat dissipation.

Received 20 July 2024; revised 5 December 2024 and 11 February 2025; accepted 15 March 2025. Date of publication 20 March 2025; date of current version 26 May 2025. Recommended for publication by Associate Editor Z. Zhang. *(Corresponding author: Akram Sheikhi.)*

Akram Sheikhi is with the Electrical Engineering Department, Lorestan University, Khorramabad 6815144316, Iran (e-mail: sheikhi.a@lu.ac.ir).

Jiteng Ma and Mark Beach are with the Department of Electrical and Electronic Engineering, University of Bristol, BS8 1TH Bristol, U.K. (e-mail: jiteng.ma@bristol.ac.uk; m.a.beach@bristol.ac.uk).

Andrei Grebennikov is with the Radio Frequency and Microwave Power Amplifier Specialist, Sumitomo Electric Europe, WD6 3SL Borehamwood, U.K. (e-mail: grandrei@ieee.org).

Color versions of one or more figures in this article are available at https://doi.org/10.1109/TPEL.2025.3553224.

Digital Object Identifier 10.1109/TPEL.2025.3553224

Switching mode PAs achieve a higher theoretical efficiency limit compared to transconductance mode PAs. The Class-E PA, a type of switching mode PA, was initially proposed by Ewing and has since gained widespread adoption due to its high-efficiency operation and simple topology [5]. Sokal and Sokal introduced the first Class-E PA design, which features a shunt capacitor and a series resonant circuit connected to the transistor [6], [7].

The key to minimizing power dissipation in Class-E PAs is to prevent the simultaneous occurrence of high voltage and current in the transistor, particularly during switching transitions. When the transistor turns OFF, it can potentially draw a high current. To minimize losses, the voltage across the transistor should ideally be zero at this point, which can be achieved through zero-voltage switching (ZVS) conditions. When the transistor turns ON, not only should the voltage be zero, but its rate of change should also be zero to further reduce switching losses. This is accomplished by applying zero derivative voltage switching (ZDVS) conditions. However, Class-E PAs typically generate very high-voltage swings across the transistor. This characteristic poses a significant reliability concern, as these voltage excursions may exceed the safe operating area limits of the devices.

The high-efficiency inverse Class-E PA represents a variant designed to achieve optimal power efficiency while minimizing distortion characteristics. The inverse Class-E PA with a series filter, initially proposed by Mury [8] and elaborated upon in subsequent studies [9], has gained significant popularity. The output waveform of the inverse Class-E operation is the complement or inverse of the waveforms of Class-E PA. Rather than utilizing ZVS and ZDVS as in Class-E PAs, achieving high efficiency of inverse Class-E PA is facilitated by employing zero-current switching (ZCS) and zero-derivative current switchings (ZDCS) conditions. These conditions enable soft switching during the ON-to-OFF transition, effectively reducing switching losses associated with current. To design a high-efficiency inverse Class-E PA, several techniques and considerations have been introduced in [8] and [9]. This design is favored for its lower maximum switch voltage than Class-E amplifiers and its high efficiency.

Inverse Class-E PA has a 20% lower peak switch voltage than Class-E, as well as can absorb device output inductance. However, early inverse Class-E topology employs a large, lossy, and bulky L_{RFC} choke, as shown in Fig. 1(a). The effect of the bond wire inductance is mentioned in [10] and [11], and the effect of ON resistance and parasitic output capacitance

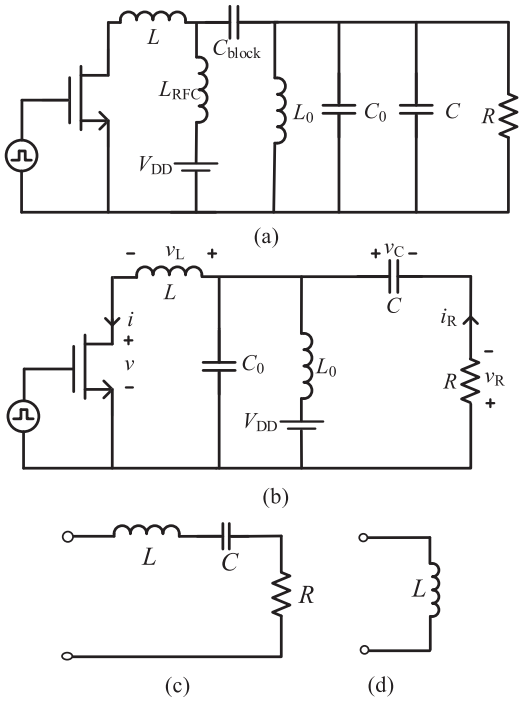

Fig. 1. (a) Conventional inverse Class-E. (b) Proposed inverse Class-E PA. (c) Load network of the proposed PA at the fundamental frequency. (d) Load network of the proposed PA at the harmonic frequencies.

are presented in [12]. The performance of inverse Class-E PA based on ZCS and ZDCS conditions has been discussed in [13], and its performance at any duty ratio has been compared with Class-F_3/E PA.

This article proposes an innovative inverse class-E PA, where a circuit topology incorporating a finite inductor is introduced to replace the traditionally bulky L_{RFC} chock. The key contributions of this article are listed as follows.

1) Proposed an innovative inverse Class-E PA provides a comprehensive analysis.
2) The idealized waveforms and load parameters have been verified to achieve 100% efficiency.
3) The proposed architecture has been designed using both lumped elements and distributed transmission line circuits to fulfill the operation condition.

The rest of this article comprehensively explains the circuits analysis, simulation and implementation process, and research findings. Section II provides a detailed description of the inverse Class-E analysis, focusing on various aspects of the circuit. It includes the derivation of the current and voltage waveforms. Section III covers the simulation and implementation of two circuit prototypes. One circuit prototype utilizes a gallium nitride (GaN) high-electron-mobility transistor (HEMT) CGH40010F with a lumped-element load network at 430 MHz. Also, Section III provides details of the implementation process and highlights the specific components and configurations used for the transmission line inverse Class-E prototype at 2.4 GHz. Section IV provides a concise overview of the contributions and concludes this article.

II. Analysis of the Proposed Inverse Class-E Amplifier

The configurations of the conventional inverse Class-E and proposed inverse Class-E amplifiers are depicted in Fig. 1(a) and (b), respectively. Fig. 1(b) illustrates that the proposed PA exhibits different impedance properties from conventional inverse Class-E designs. The load networks of the proposed PA at the fundamental and harmonic frequencies are presented in Fig. 1(c) and (d), respectively. It is evident that the inverse Class-E mode with a shunt filter at the fundamental frequency demonstrates distinct impedance properties compared to an alternative inverse Class-E configuration with a series filter. At both even and odd harmonics, its optimum impedances can be determined by the series L, akin to the inverse Class-E in Fig. 1(a). The proposed PA offers the advantage of the following.

1) It can mitigate the influence of transistor output inductance, particularly noticeable at higher frequencies.
2) Finite inductor L_0 instead of infinite inductor L_{RFC} in the conventional inverse Class-E, which is bulky and lossy, results in a more compact circuit.
3) The basic advantage of the proposed inverse Class-E is the significantly lower drain voltage peak, 2.86 instead of 3.56 for a conventional Class-E, which significantly reduces the requirement for device breakdown voltage.
4) The proposed inverse Class-E amplifier does not require any dc blocking capacitance, unlike the conventional inverse Class-E PA in Fig. 1(a). This results in a simpler structure and improved design.
5) The analyzed maximum operating frequency surpasses those reported in other publications, making the proposed design well-suited for operation in the microwave frequency range.

In this analysis, the switch operates in an OFF state during $0 < \omega t < \pi$ and in an ON state during $\pi < \omega t < 2\pi$. Similar to the conventional inverse Class-E PA, the switch current satisfies the ZCS conditions as

$$i(\omega t)\,|_{\omega t=2\pi} = 0$$
$$\frac{di(\omega t)}{d\omega t}\,|_{\omega t=2\pi} = 0. \tag{1}$$

The load current is defined as

$$i_R(\omega t) = I_R \sin(\omega t + \phi). \tag{2}$$

Here, ϕ represents the initial phase shift of the current. During $0 < \omega t < \pi$, the switch is in the OFF state, resulting in zero voltage across the inductor L. Therefore

$$v(\omega t) = v_C(\omega t) - v_R(\omega t), \;\; v(0) = 0 \tag{3}$$

and the voltage $v_C(\omega t)$ between the capacitance C can be expressed by current I_R flowing through the capacitance C as

$$v_C(\omega t) = -\frac{1}{\omega C}\int_0^{\omega t} I_R \sin(\omega t + \phi) d\omega t + v_C(0). \tag{4}$$

Considering (4), the voltage $v_C(0)$ can be obtained from $v(0) = 0$ as

$$v_C(0) = \text{R}I_R \sin\phi. \tag{5}$$

Using (3)–(5), the switch voltage is obtained as

$$v(\omega t) = \mathrm{RI}_R \times \left[\begin{array}{l} \langle \sin\phi - \sin(\omega t+\phi)\rangle \\ +\frac{1}{\omega \mathrm{CR}} \langle \cos(\omega t+\phi) - \cos\phi\rangle \end{array} \right]. \quad (6)$$

For $\pi < \omega t < 2\pi$, the voltage of inductor L can be obtained as

$$v_L(\omega t) = v_C(\omega t) - v_R(\omega t). \quad (7)$$

Equation (7) can be represented as

$$\omega L \frac{di}{d\omega t} = \frac{-I_R}{\omega C} \int_{\pi}^{\theta} \sin(\omega t+\phi) d\omega t + v_C(\pi) - \mathrm{RI}_R \sin(\omega t+\phi). \quad (8)$$

The voltage $v_C(\pi)$ can be obtained from $v_L(\pi) = v(\pi)$ as

$$v_C(\pi) = -\frac{2}{\omega C} I_R \cos\phi + \mathrm{RI}_R \sin\phi. \quad (9)$$

Solving (8), the normalized switch current is obtained as

$$\omega L \frac{di}{d\omega t} = \mathrm{RI}_R \left\{ \langle \sin\phi - \sin(\omega t+\phi)\rangle + \frac{1}{\omega \mathrm{CR}} \cos(\omega t+\phi) \right\}. \quad (10)$$

The general solution is in the form of

$$i(\omega t) = I_R \times \left\{ \begin{array}{l} q^2[\sin(\omega t+\phi) + \sin\phi + \pi\cos\phi - \omega t\cos\phi] \\ + \left[\frac{\cos(\omega t+\phi)+\cos\phi+\omega t\sin\phi-\pi\sin\phi}{\omega L/R} \right] \end{array} \right\} \quad (11)$$

where

$$q = 1/\omega\sqrt{\mathrm{LC}}.$$

The voltage V_{DD} and current I_{DD} can be determined by applying Fourier-series expansion to (6) and (11) as

$$V_{\mathrm{DD}} = \frac{1}{2\pi} \int_0^{\pi} v(\omega t) d\omega t = \frac{\mathrm{RI}_R}{2\pi} \left\{ \left\langle \frac{2-\pi\omega\mathrm{CR}}{\omega\mathrm{CR}} \right\rangle \sin\phi + \left\langle \frac{\pi+2\omega\mathrm{CR}}{\omega\mathrm{CR}} \right\rangle \cos\phi \right\} \quad (12)$$

and

$$I_{\mathrm{DD}} = \frac{1}{2\pi} \int_{\pi}^{2\pi} i(\omega t) d\omega t = I_R \times \left\{ \begin{array}{l} q^2 \left\langle \frac{1}{2}\sin\phi - \frac{\pi^2+4}{4\pi}\cos\phi \right\rangle + \\ \frac{R}{\omega L} \left\langle \frac{1}{2}\cos\phi + \frac{\pi^2+4}{4\pi}\sin\phi \right\rangle \end{array} \right\}. \quad (13)$$

The peak switch voltage $V_{\max}$ and current $I_{\max}$ can be determined from (6) and (11) using (12) and (13) as

$$\frac{V_{\max}}{V_{\mathrm{DD}}} = 2.86 \quad (14)$$

$$\frac{I_{\max}}{I_{\mathrm{DD}}} = 3.56. \quad (15)$$

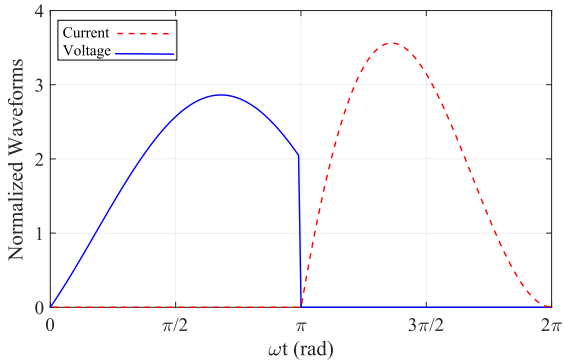

Fig. 2. Ideal normalized switch voltage and current waveforms from the theoretical analysis.

The definition of the output power capability c_p is expressed as

$$c_p = \frac{1}{\left|\frac{V_{\max}}{V_{\mathrm{DD}}}\right|\left|\frac{I_{\max}}{I_{\mathrm{DD}}}\right|} = 0.0982. \quad (16)$$

Equation (14) shows that the normalized voltage peak factor of the proposed inverse Class-E PA is lower than that of the conventional Class-E PA. The voltage waveforms from (6) and the current waveforms from (11) are plotted using Mathcad software. Fig. 2 illustrates the normalized voltage and current waveforms over the interval $0 < \omega t < 2\pi$.

The fundamental-frequency current through the switch comprises two quadrature components, where the amplitude of the real component is defined by the Fourier formula as

$$I_R = -\frac{1}{\pi} \int_0^{2\pi} i(\theta) \sin(\theta+\phi) d\theta. \quad (17)$$

For the efficiency of 100%, the dc power $P_{\mathrm{dc}} = V_{\mathrm{DD}} I_{\mathrm{DD}}$ and the output power $P_{\mathrm{out}} = R I_R^2/2$ are equal, which can be expressed as

$$V_{\mathrm{DD}} I_{\mathrm{DD}} = \mathrm{RI}_R^2/2. \quad (18)$$

Using q, (12)–(13), and (15), the equation for the normalized capacitance C can be derived as

$$\omega\mathrm{CR} = -\frac{2\sin\phi - \pi\cos\phi}{2\cos\phi + \pi\sin\phi}. \quad (19)$$

Subsequently, $\omega L/R$ can be derived from q and (19) as

$$\frac{\omega L}{R} = \frac{1}{\omega\mathrm{CR} \times q^2}. \quad (20)$$

As a result, by solving a system of three equations—two inverse Class-E switching conditions given by (1) and the third one for I_R given by (17)—the three unknown parameters can be calculated as

$$q = 1.412 \quad (21)$$

$$\phi = 15^\circ \quad (22)$$

$$\frac{I_R}{I_{\mathrm{DD}}} = 1.65. \quad (23)$$

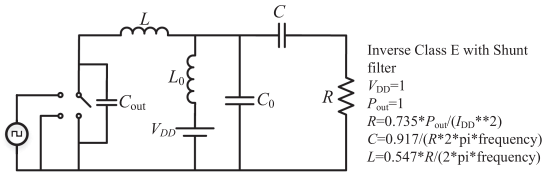

Fig. 3. Simulation setup in the frequency domain using Keysight ADS.

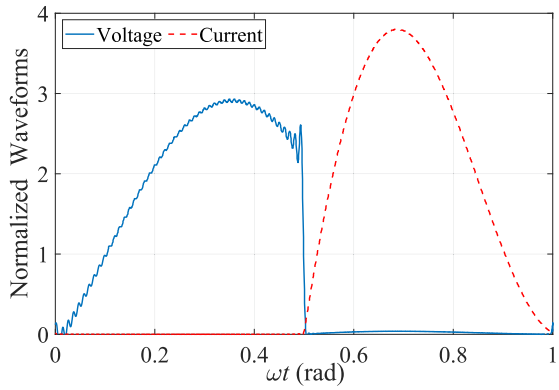

Fig. 4. Normalized waveforms in the frequency domain with $\omega C_{\text{out}}R$=0.

Thus, the ωCR=0.913 and $\omega L/R$=0.549 have been obtained. The optimum load resistance R can be obtained as

$$R = \frac{2\,P_{\text{out}}}{I_R^2} = 2\left(\frac{I_{\text{DD}}}{I_R}\right)^2 \frac{P_{\text{out}}}{I_{\text{DD}}^2}. \tag{24}$$

From Fig. 1(c), the phase angle φ is obtained as

$$\varphi = \tan^{-1}\left(\frac{\omega^2\,\text{LC}-1}{\omega\text{CR}}\right). \tag{25}$$

The maximum operating frequency $f_{\max}$ can be obtained from (24) and ωCR=0.913 as

$$f_{\max} = 0.186\frac{I_{\text{DD}}^2}{CP_{\text{out}}}. \tag{26}$$

Fig. 3 shows the nominal inverse Class-E PA simulation setup in Keysight advanced design system (ADS), utilizing an input pulse source in the frequency domain. It is worth noting that, in this simulation setup, the transistor is modeled as an ideal switch to facilitate theoretical analysis, whereas real devices include parasitics that cause finite switching times. This serves as an approximation to ideal conditions, with the transistor operating as a multiharmonic current source in saturation under slightly overdriven conditions. To accurately simulate the nonlinear behavior of the switching-mode inverse Class-E PA, the number of harmonics was set to 16 considering the sharp transitions in pulse signals during the transient simulation. Based on the simulation setup in Fig. 3, the normalized switch voltage and current waveforms of the idealized inverse Class-E PA with $\omega C_{\text{out}}R$=0 are shown in Fig. 4. However, the simulation waveforms for the optimum load-network parameters may not be accurate due to the choice of finite harmonic components.

The voltage and current waveforms of the transistor because of the existence of the parasitic output capacitance C_{out} is changed.

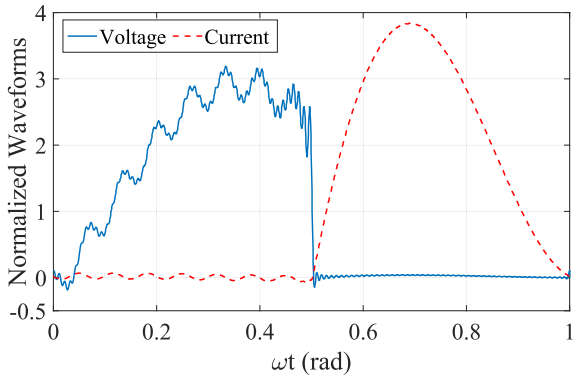

Fig. 5. Drain voltage and current with output capacitance $\omega C_{\text{out}}R$.

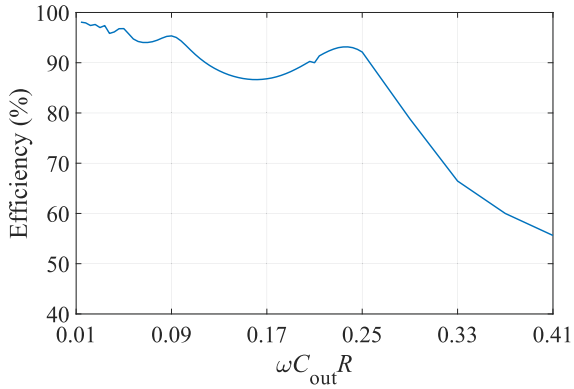

Fig. 6. Drain efficiency as a function of output capacitance $\omega C_{\text{out}}R$.

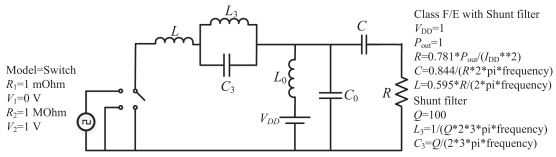

Fig. 7. Schematic of the proposed Class-F/E PA.

The waveforms shown in Fig. 5 show that the optimum operation conditions are close to optimal. Here, to investigate the effect of the transistor's shunt capacitor, the harmonic balance simulation result of various shunt capacitance is given in Fig. 6. The results indicate that drain efficiency does not monotonically decrease with increasing output capacitance. Interestingly, the inverse Class-E PA demonstrates higher efficiency at larger values of $\omega C_{\text{out}}R$ compared to certain lower values.

To minimize the current peak factor, the load network parameters can be adjusted to align with the Class-F_3/E mode, as shown in Fig. 7. This involves configuring the third-harmonic tank L_3-C_3 in series with the series inductance L to achieve an open-circuit condition at the third harmonic. Fig. 8 illustrates the ideal and simulated drain voltage and current waveforms. However, due to the sufficiently low-quality factor of the third-harmonic resonator, efficiency drops. To address this, the proposed load network with a shunt filter can be modified to operate in Class-F_3/E mode without power loss at harmonics. As demonstrated in Fig. 9, the shape of the voltage waveform of

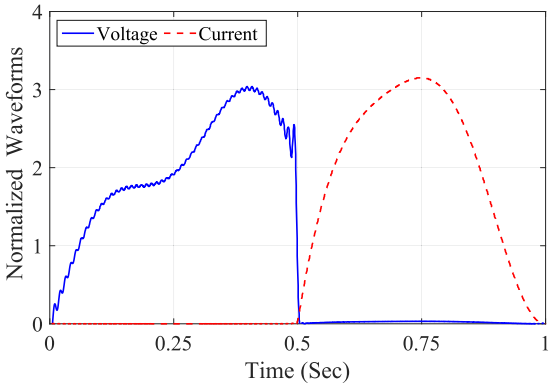

Fig. 8. Simulated waveforms of the proposed inverse Class-F/E PA.

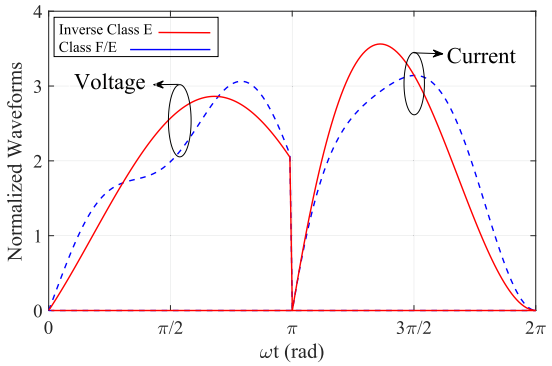

Fig. 9. Simulated waveforms comparison between the proposed inverse Class-E and Class-F/E PAs.

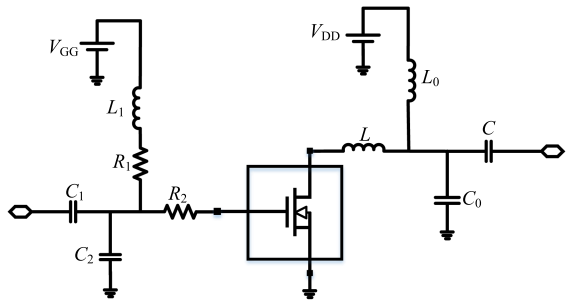

Fig. 10. Basic schematic of the proposed PA.

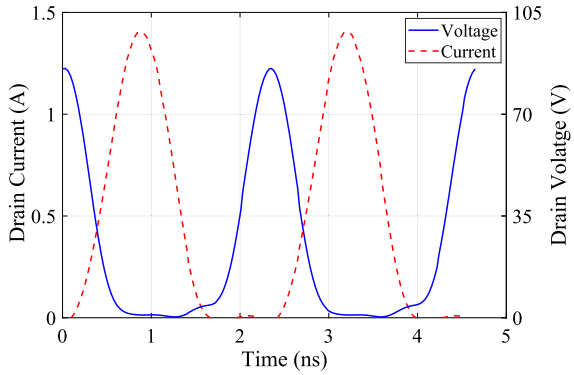

Fig. 11. Simulated intrinsic current and voltage waveforms of the proposed inverse Class-F/E PA using realistic transistor model.

inverse Class-E is influenced by the resonant network, typically L_3-C_3 tank circuit, which helps shape the waveform and filter out undesired harmonic components. The drain voltage waveform in the Class-F/E mode in Fig. 9 typically exhibits switching transitions.

III. Simulation and Measurement Results of the Inverse Class-E PA

A. Lumped Element Inverse Class-E PA

The application of the developed theoretical framework and its practical implications for circuit design are subsequently presented. First, we elaborate on the design of an inverse Class-E PA prototype at 430 MHz. The PA is implemented using a CGH40010F GaN HEMT transistor. The circuit schematic used in the simulation is shown in Fig. 10. The design example is subjected to the specifications, i.e., $f_0 = 430$ MHz, $P_{\text{out}} = 12$ W, and $Q = 10$. The values of the parameters calculated from analytical equations for the proposed inverse Class-E are $L_0 = 1.89$ nH, $C_0 = 72.51$ pF, $L = 10.34$ nH, $C = 6.65$ pF, and $R = 51\ \Omega$. In the simulation setup, the specification parameters of the proposed PA are as follows: $D = 0.5$, $f_0 = 430$ MHz, $C_0 = 72$ pF, $L_0 = 1.9$ nH, $R = 50\ \Omega$, $L = 8.34$ nH, $C = 6.24$ pF, and $V_{\text{DD}} = 28$ V for load network and $R_1 = 88\ \Omega$, $R_2 = 12\ \Omega$, $L_1 = 15$ nH, $C_1 = 104$ pF, $C_2 = 13.3$ pF, and $V_{\text{GG}} = -2.89$ V for input matching circuit. The simulated waveforms of the designed inverse Class-E PA using the realistic transistor model are shown in Fig. 11. The negative part of the current across the inductor results from the discharging inductor process during the half period when the switches are turned-ON. Voltage does not drop instantly at $\omega t = \pi$ because it still continues to flow through C_{out} when the switch is turned-OFF.

B. Transmission Line Inverse Class-E PA

To achieve a transmission line load network that aligns with the inverse Class-E mode, it is crucial to carefully select optimal parameters such as C, L, and R at the fundamental frequency. In addition, appropriate inductance at the second and third harmonics should be incorporated. Fig. 12(a) illustrates the designed load network, detailing the electrical characteristics of the transmission lines and the specifications of the packaged elements. Since the transistors used in this study are commercially packaged, these elements must be integrated into the load network design. The equivalent circuit of the load network at the second and third harmonic frequencies are shown in Fig. 12(b) and (c), respectively. Smith chart in Fig. 12(d) depicts theoretical and simulated load impedances at the first three harmonics. Inductance terminations at 4.8 GHz and 7.2 GHz and the required fundamental-frequency impedance at 2.4 GHz are met.

Fig. 13 presents the schematic of the designed PA operating at 2.4 GHz, including the dimensions of its elements. All simulations during the design process were conducted using ADS

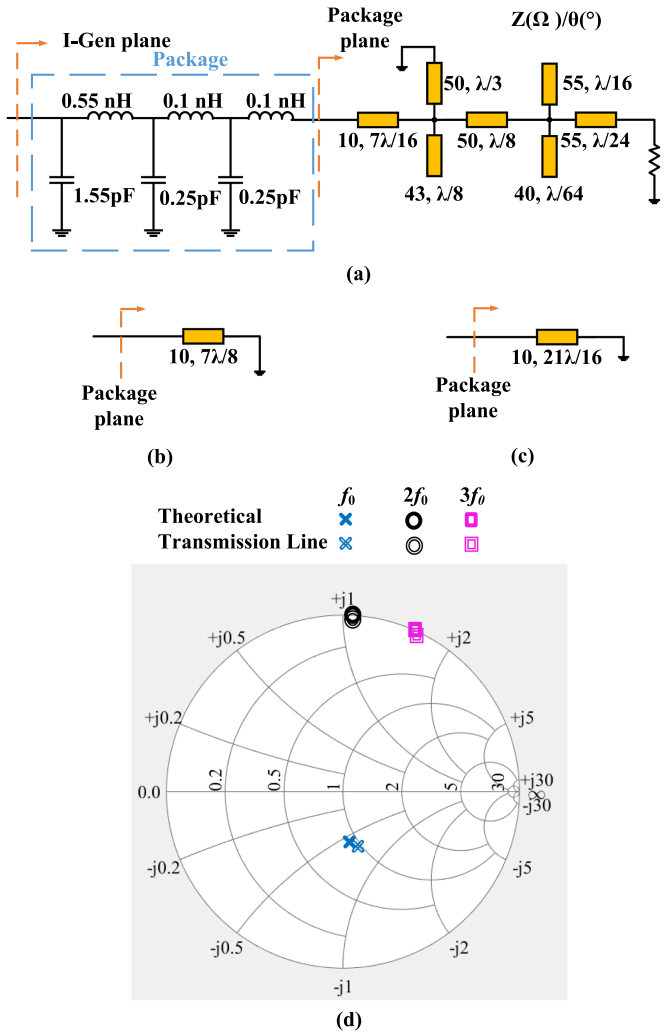

Fig. 12. Schematic of the load network at (a) fundamental frequency, (b) second, (c) third harmonic frequencies, and (d) theoretical and simulated load impedances.

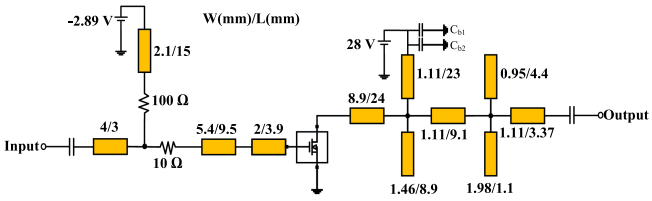

Fig. 13. Schematic circuit of the designed PA prototype.

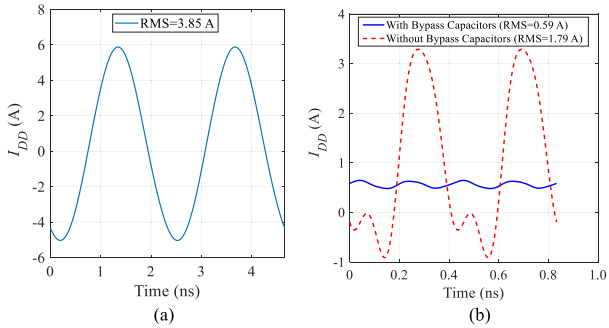

Fig. 14. DC current going from the DC source (a) Fig. 10. (b). Fig. 13.

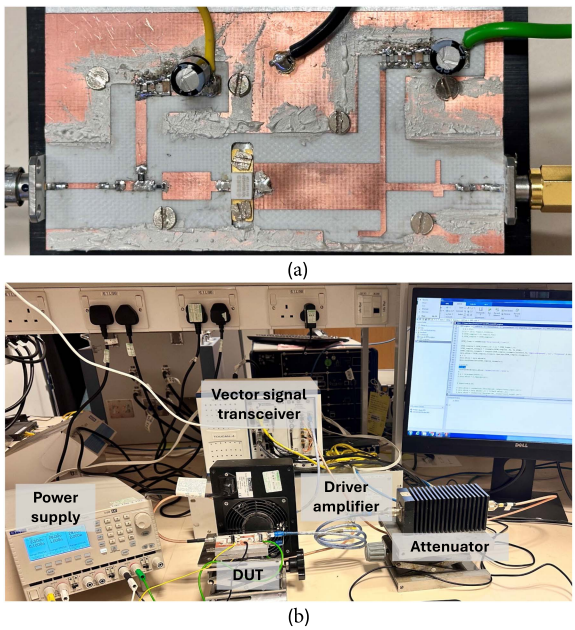

Fig. 15. (a) Photograph of the fabricated PA DUT. (b) Measurement setup.

2022. As the dc-feed inductor also performs part of the load network of the proposed PA, it is necessary to incorporate the current waveforms and rms value estimation for the input current going from the dc source. The schematic in Fig. 3 represents an ideal case where the parallel inductor and shunt capacitor have infinite self-Q, leading to high RF current amplitudes as current circulates within the parallel filter circuit. However, in real-world conditions, a more practical approach is to analyze the current waveform using a realistic device—specifically through L_0 in Fig. 10 and the drain line current in Fig. 13. In Fig. 10, the inductor has a finite self-Q of approximately 10 due to parasitic series resistance. Its actual value also depends on the loaded Q, which is set to 10 in our case but may be lower in some scenarios. In Fig. 13, the presence of a bypass capacitor C_{b1} and C_{b2} significantly reduces the input current from the dc source. Fig. 14 presents the input current waveforms and rms value estimations from the dc source for all three cases. However, this does not pose an issue for the lumped devices. A more reliable solution is to use a wire with an appropriate diameter that meets the fusing current requirements. The designed PA is fabricated on a Rogers RO4003C PCB substrate with a thickness of 0.508 mm, as shown in Fig. 15(a), with the measurement setup depicted in Fig. 15(b). Large-signal continuous wave (CW) measurements for power and efficiency characterization, as well as modulated signal measurements for linearity testing, are conducted using a National Instruments PXIe-5646R vector signal transceiver (VST). The carrier frequency range extends up to 6 GHz, with high-speed digital input/output (I/O) capabilities of up to 250 Mb/s. The VST is used to generate both CW and modulated signals within this frequency range. The input power

TABLE I
COMPARISON WITH THE STATE-OF-THE-ART

	This work	[8]	[12]	[13]	[14]	[15]	[16]	[17]
Circuit topology	**Class-E^{-1}**	Class-E^{-1}	Class-E^{-1}	Class-F/E	Class-F/E	Class-E	Class-E/F	Class-E/F
Frequency (GHz)	**2.4**	2.5	2.3	2.21	0.004	1.37	2.3	0.0008
Output resonant filter	**Parallel**	Parallel	Parallel	Series	Parallel	Parallel	Parallel	Series
Component number	**4**	6	6	9	8	6	6	6
Switching type	**ZCS**	ZCS	ZCS	ZCS	ZCS	ZVS	ZVS	ZVS
V_{max}/V_{DD}	**2.86**	2.86	2.86	3.056	3.056	2.86	3.14	3.14
Normalized f_{max}	**0.186**	0.106	0.106	0.072	0.1	0.097	0.0698	0.0506
Power output capability	**0.098**	0.098	0.098	0.1057	0.1041	0.097	0.1046	-
Output power (W)	**11.7**	0.5	0.158	10	12	9.54	13.8	1
Drain efficiency (%)	**82**	66	69	83	90	90.2	83.9	94.6

The bold values highlight the results related to our work in comparison to other PAs.

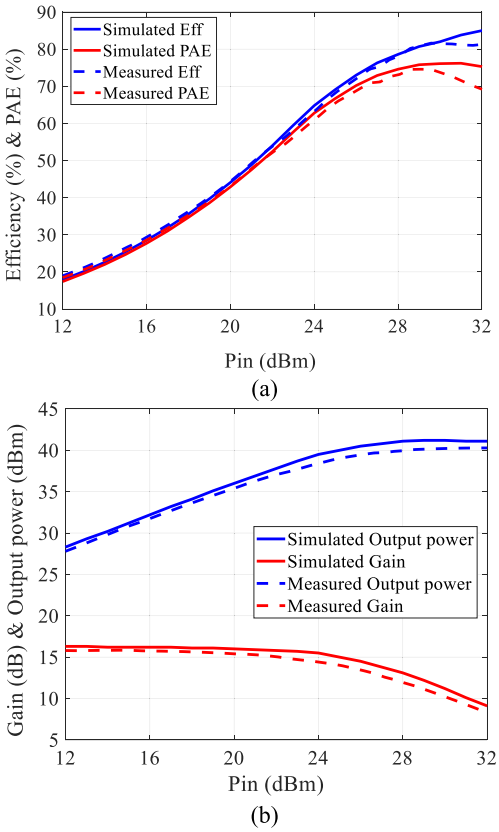

Fig. 16. Simulated and measured results of the designed PA versus input power.

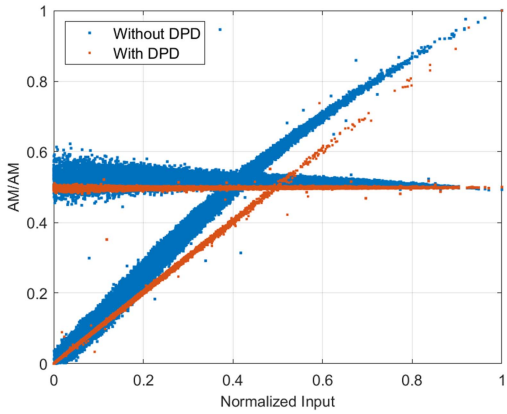

Fig. 17. Measured A.M./A.M. and A.M./P.M. before and after DPD.

is first amplified by a 35 W EMPOWER driving amplifier and then amplified by the device under test (DUT). Before feeding the signal back to the VST, the output of the PA is connected to an attenuator. The simulated and measured drain efficiency, power added efficiency (PAE), output power, and gain of the designed PA are shown in Fig. 16. This proposed PA achieves the drain efficiency and PAE of 82% and 75%, respectively. The maximum output power is 40.5 dBm with a saturation gain of 11.0 dB at the input power of 30 dBm. For evaluating the performances of the proposed design, the fabricated PA is tested with CW signals. Like the simulation, the measurement is also performed at 2.4 GHz. During the measurement, the quiescent current and gate voltage of the inverse Class-E PA is set to 50 mA, and −2.42 V, respectively.

Table I summarizes the designed inverse Class-E PA and compares it to the state-of-the-art PAs. The proposed PA provides a good performance comparable to contemporary designs. This work utilizes a parallel output resonant filter, while [8], [12], [14], [15], and [16] also implement parallel filters. In contrast, the authors in [13] and [17] employed series filters in their designs. The design presented in this work features four components, which is lower than other configurations. This reduction in component number not only simplifies the design but also offers potential benefits regarding component stress. However, it has a lower maximum switch voltage compared to [13], [14], [16], and [17]. By utilizing only four components, this design simplifies the circuit, reducing complexity and potential points of failure. The absence of the L_{RFC} simplifies the overall design, reducing manufacturing costs and complexity, which distinguishes it from studies [8], [12], [13], [14], and [17], which integrate L_{RFC} components into their designs. Conversely, Liu and Cheng [16] also omited this component but has a higher maximum switch voltage V_{max}. The proposed inverse Class-E PA has a relatively low V_{max}, making it more compatible with monolithic microwave integrated circuit technology. The proposed structure achieves a maximum operating frequency f_{max} that is 1.75 times higher than those reported in [8] and [12], 2.58 times higher than [13], 1.86 times higher than [14], 1.92 times higher than [15], 2.66 times higher than [16], and 3.67 times higher than [17]. With

a higher f_{max}, the proposed inverse Class-E PA is well-suited for operation in the microwave frequency range. It is necessary to clarify that the component counts for the different PAs listed in Table I do not include electromagnetic interference filters.

Fig. 17 shows the measured amplitude-to-amplitude modulation (A.M.–A.M.) and amplitude-to-phase modulation (A.M.–P.M.) performance with and without digital predistortion (DPD) under 40 MHz orthogonal frequency division multiplexing (OFDM) signals at 2.4 GHz. In terms of A.M.–A.M performance, the graph shows how output amplitude varies relative to input amplitude. Without DPD, the A.M.–A.M curve typically displays a nonlinear response as input amplitude increases. This nonlinearity indicates that the amplifier begins to compress at higher input levels, leading to signal distortion. With DPD applied, however, the A.M.–A.M response becomes more linear. The DPD corrects the gain compression, allowing the amplifier to maintain a more consistent output amplitude across a range of input levels, which significantly reduces amplitude-related distortion in the transmitted signal. The A.M.–P.M. performance illustrates how phase shift varies with changes in input amplitude. Without DPD, the A.M.–P.M. curve typically shows increasing phase deviation as the input amplitude rises, a common result of nonlinearities within the PA. This phase deviation contributes to signal distortion, affecting the accuracy of the transmitted data. When DPD is applied, the A.M.–P.M. curve becomes more stable, with reduced phase shift over varying input amplitudes. This improvement minimizes phase-related distortion and enhances the fidelity of the transmitted signal.

IV. Conclusion

In this article, the theoretical analysis of an inverse Class-E PA with a shunt filter has been presented. The ideal voltage and current waveforms, as well as the load network parameters, have been confirmed via frequency-domain simulations. High efficiency and output power capability are ensured by evaluating performance under ZCS and ZCDS conditions. The findings reveal that the maximum switch voltage is lower than in conventional Class-E designs. In addition, utilizing a finite inductor L_0 instead of an infinite inductor L_{RFC} in the conventional inverse Class-E yields a more compact circuit. The theoretical analysis through simulation and test results for both lumped element and transmission line PAs have been validated. The high drain efficiency and PAE of 82% and 75% at 30-dBm input power is achieved for the transmission line inverse Class-E configuration.

References

[1] H. Viswanathan, S. Wesemann, J. Du, and H. Holma, "Energy efficiency in next-generation mobile networks," White Paper, Nokia Bell Labs, Murray Hill, NJ, USA, Nov. 2022.

[2] A. Grebennikov, N. O. Sokal, and M. J. Franco, *Switchmode RF and Microwave Power Amplifiers*. Newnes, NSW, Australia: Academic Press, 2021.

[3] R. Quaglia, J. Pang, S. C. Cripps, and A. Zhu, "Load-modulated balanced amplifier: From first invention to recent development," *IEEE Microw. Mag.*, vol. 23, no. 12, pp. 60–70, Dec. 2022.

[4] J. Ma et al., "Highly efficient 3-Bit digital power amplifier for OFDM waveform amplification," *IEEE Trans. Microw. Theory Techn.*, vol. 71, no. 1, pp. 35–47, Jan. 2023.

[5] G. D. Ewing, "High-efficiency radio-frequency power amplifiers," Ph.D. dissertation, Dept. Elect. Eng., Oregon State Univ., Corvallis, OR, USA, 1964.

[6] N. O. Sokal and A. D. Sokal, "Class E—A new class of high-efficiency tuned single-ended switching power amplifiers," *IEEE J. Solid-State Circuits*, vol. SSC-10, no. 3, pp. 168–176, Jun. 1975.

[7] F. Raab, "Idealized operation of Class E tuned power amplifier," *IEEE Trans. Circuits Syst.*, vol. CAS-24, no. 12, pp. 725–735, Dec. 1977.

[8] T. Mury and V. F. Fusco, "Series-L/parallel-tuned comparison with shunt-C/series-tuned Class-E power amplifier," *IEE Proc. Circuits, Devices Syst.*, vol. 152, no. 6, pp. 709–717, Dec. 2005.

[9] T. Mury and V. F. Fusco, "Inverse Class-E amplifier with transmission line harmonic suppression," *IEEE Trans. Circuits Syst. I. Reg. Papers*, vol. 54, no. 7, pp. 1555–1561, Jul. 2007.

[10] H. Jäger, A. Grebennikov, E. Heaney, and R. Weigel, "Broadband high-efficiency monolithic in InGaP/GaAs HBT power amplifiers for wireless applications," *Int. J. RF Microw. Comput.-Aided Eng.*, vol. 13, no. 6, 496–510, 2003.

[11] T. Mury and V. F. Fusco, "Inverse Class-E amplifier with transmission-line harmonic suppression," *IEEE Trans. Circuits Syst. I: Reg. Papers*, vol. 54, no. 7, 1555–1561, Jul. 2007.

[12] T. Mury and V. F. Fusco, "Sensitivity characteristics of inverse Class-E power amplifier," *IEEE Trans. Circuits Syst. I: Reg. Papers*, vol. 54, no. 4, 768–778, Apr. 2007.

[13] A. Sheikhi, M. Hayati, and A. Grebennikov, "High-efficiency Class-E^{-1} and Class-F/E power amplifiers at any duty ratio," *IEEE Trans. Ind. Electron.*, vol. 63, no. 2, pp. 840–848, Feb. 2016.

[14] A. Sheikhi and H. Hemesi, "Analysis and design of the novel Class-F/E power amplifier with series output filter," *IEEE Trans. Circuits Syst. II: Reg.*, vol. 69, no. 3, pp. 779–783, Mar. 2022.

[15] M. S. Mugisho et al., "Generalized Class-E power amplifier with shunt capacitance and shunt filter," *IEEE Trans. Microw. Theory Techn.*, vol. 67, pp. 3464–3474, Aug. 2019.

[16] C. Liu and Q-F. Cheng, "Analysis and design of high-efficiency parallel-circuit Class-E/F power amplifier," *IEEE Trans. Microw. Theory Techn.*, vol. 67, pp. 2382–2392, Jun. 2019.

[17] S. Pezeshkpour and M. M. Ahmadi, "Design procedure for a high-efficiency Class-E/F_3 power amplifier," *IEEE Trans. Power Electron.*, vol. 38, no. 11, pp. 14388–14399, Nov. 2023.

Akram Sheikhi (Senior Member, IEEE) received the B.Sc. degree in electronic engineering from Shariaty University, Tehran, Iran, in 2007 and the M.Sc. and Ph.D. degrees in electrical engineering from Razi University, Kermanshah, Iran, in 2010 and 2015, respectively.

In October 2015, she was an Assistant Professor of Electrical Engineering with Lorestan University, where she became an Associate Professor, in June 2020. She is involved in the university's courses, such as circuits, electronics, high-frequency integrated circuits, monolithic microwave integrated circuits, and computer-aided design. She has authored or coauthored widely in these areas, including journal articles, research, and practical projects. Her current research interests include the design of high-efficiency RF and microwave power amplifiers, the design of passive circuits, and the design of wireless power transfer systems and energy harvesting.

Dr. Sheikhi was the recipient of the Scholarship from Lorestan University, Khorramabad, Iran, in April 2014.

Jiteng Ma (Member, IEEE) received the B.Eng. degree in mechanical engineering from the Beijing University of Posts and Telecommunications, Beijing, China, in 2014, and the M.Sc. degree in communication networks and signal processing and Ph.D. degree in electrical and electronic engineering from the University of Bristol, Bristol, U.K., in 2019 and 2024, respectively.

He is currently a Senior Research Associate with the University of Bristol. His research focuses on the design of RF power amplifiers and RF-oriented machine learning technologies.

Andrei Grebennikov (Senior Member, IEEE) received the Dipl. Eng. degree in radio electronics from the Moscow Institute of Physics and Technology, Moscow, Russia, in 1980, and the Ph.D. degree in radio engineering from the Moscow Technical University of Communications and Informatics, Moscow, Russia, in 1991.

He obtained a long-term academic and industrial experience working with the Moscow Technical University of Communications and Informatics, Moscow, Russia, the Institute of Microelectronics, Singapore, M/A-COM, Cork, Ireland, Infineon Technologies, Munich, Germany, and Linz, Austria, Bell Labs, Alcatel-Lucent, Dublin, Ireland, and Microsemi, Aliso Viejo, California, Sumitomo Electric Europe, Elstree, U.K., as an Engineer, Researcher, Lecturer, and Educator. He has lectured as a Guest Professor with the University of Linz, Linz, Austria. He is an author and coauthor of more than 100 papers, holds 30 European, and U.S. patents, and has authored 10 books dedicated to RF and microwave circuit design.

Dr. Grebennikov presented short courses and tutorials as an Invited Speaker at the IEEE Microwave Theory and Techniques Society (MTT-S) International Microwave Symposia (IMS), European and Asia-Pacific Microwave Conferences, the Institute of Microelectronics, Singapore, Motorola Design Centre, Penang, Malaysia, the Tomsk State University of Control Systems and Radioelectronics, Tomsk, Russia, and the Aachen Technical University, Aachen, Germany.

Mark Beach (Senior Member, IEEE) received the B.Sc. degree in electronic engineering from the University of York and the Ph.D. degree from the University of Bristol, UK, in 1983 and 1988, respectively. Has more than 35 years of experience in physical layer wireless research and RF enabling technologies, including resilient and energy efficient RF transceivers. Much of his research is experimentally driven in order to facilitate real-world deployments through proof of concept demonstrators and parameter optimization alongside enhancing circuit and system level models. He leads the delivery of the UKRI/EPSRC SWAN Prosperity Partnership in Secure Wireless Agile Networks, RF PA research within the U.K. DSIT REASON project as well as other RF related projects with industry and government. He is also the joint head of the Communication Systems and Networks Research Group, University of Bristol, Bristol, U.K. He is a co-founder of the Cambridge-based company, ForeFrontRF developing highly compact tunable duplexers.